Research Article

Unconventional energetics of small vacancy clusters in BCC high-entropy alloy Nb$_{0.75}$ZrTiV$_{0.5}$

Tan Shi [a], Xi Qiu [b], Yundi Zhou [a], Sixin Lyu [a], Jing Li [a], Dan Sun [b], Qing Peng [c,d], Yong Xin [b,*], Chenyang Lu [a,e,*]

[a] School of Nuclear Science and Technology, Xi'an Jiaotong University, Xi'an 710049, China
[b] Nuclear Power Institute of China, Chengdu 610213, China
[c] State Key Laboratory of Nonlinear Mechanics, Institute of Mechanics, Chinese Academy of Sciences, Beijing 100190, China
[d] School of Engineering Sciences, University of Chinese Academy of Sciences, Beijing 100049, China
[e] State Key Laboratory of Multiphase Flow in Power Engineering, Xi'an Jiaotong University, Xi'an 710049, China

ARTICLE INFO

ABSTRACT

The stability of small vacancy clusters including divacancy, trivacancy and tetravacancy has been studied in body-centered cubic high-entropy alloy Nb$_{0.75}$ZrTiV$_{0.5}$ in structures of random solid solution and short-range order by first-principles calculations and molecular dynamics simulations. Different from conventional body-centered cubic metals, the tightly bound configurations have a lower structural stability and are not preferred energetically in the studied high-entropy alloy. Instability of vacancy configurations leads to vacancy-atom exchanges that favor less compact configurations. The formation energy of small vacancy clusters is much smaller than its constituent elements of Nb and V due to the large structural adjustment induced by severe local lattice distortion. The difference in local lattice distortion and elemental arrangement in the vacancy neighborhood leads to significant site-to-site variation in vacancy cluster energy and configuration. The formation energy has a strong correlation with the local energy state of the vacancy configuration and the extent of structural relaxation. Compared to random solid solution, the structure of short-range order has a higher stability for the most compact cluster configurations and tends to have higher vacancy cluster formation energy. According to classical molecular dynamics simulations of cluster diffusion at high temperature, the studied high-entropy alloy has a higher probability of cluster dissociation compared to Nb and V. The unconventional energetics of small vacancy clusters is expected to have a profound impact on their generation, diffusion, dissociation, coalescence, as well as the defect microstructure evolution during irradiation.

© 2023 Published by Elsevier Ltd on behalf of The editorial office of Journal of Materials Science & Technology.

1. Introduction

High-entropy alloys (HEAs) have exhibited great radiation resistance and are considered as promising structural materials for advanced nuclear reactors [1–6]. Compared to commercial reactors, advanced reactors usually require a higher operating temperature [7–9]. This triggers the interest in the development of radiation-tolerant body-centered cubic (BCC) refractory HEAs, which intrinsically have a more suitable high-temperature performance [10,11]. Although the radiation damage studies of HEAs initiate from the scientific research of face-centered cubic (FCC)

multi-principal element alloys (MPEAs) and HEAs [1], with the rapid development of refractory HEAs, there has been growing attention to their radiation response in recent years [12]. Results from ion irradiation experiments and radiation defect simulations suggest that BCC HEAs also have promising radiation resistance including lower irradiation hardening [13,14], reduced void swelling [15] and higher defect recombination probability [16,17]. Understanding the kinetic evolution of radiation defects from defect generation to long-term defect growth requires a comprehensive understanding of the characteristics of various types of defects that take part in the process. In this work, the stability and energetics of small vacancy clusters were studied by first-principles and molecular dynamics (MD) simulations to illustrate their distinct behavior compared to conventional metals.

The superior radiation response of HEAs stems from their unique structural and chemical properties. The local lattice dis-

* Corresponding authors. School of Nuclear Science and Technology, Xi'an Jiaotong University, Xi'an 710049, China; Nuclear Power Institute of China, Chengdu 610213, China.

E-mail addresses: xinyong521raul@163.com (Y. Xin), chenylu@xjtu.edu.cn (C. Lu).

tortion and chemical disorder can greatly reduce the energy dissipation by increased electron and phonon scattering, leading to enhanced defect recombination during the displacement cascade [1,6]. The chemical disorder and chemical complexity also result in slower mobility of point defects and defect clusters. The sluggish diffusion of defects can increase the annihilation probability between vacancy and interstitial [18,19], reduce the defect clustering and growth [20], and mitigate the elemental segregation at defect sinks [3]. In addition, the defect diffusion can be tuned within the compositional space of HEAs to tailor the defect behavior [4,21,22].

In BCC HEAs, the most prominent structural difference is the more severe local lattice distortion induced by atomic size mismatch. Compared to the FCC NiCoFeCrMn alloy family, the local lattice distortion is generally ∼2–4 times larger [23,24]. Combined with the difference in chemical properties, the BCC HEAs can exhibit different defect behavior from that of the FCC counterparts. For instance, point defects have larger formation and migration energy distributions and experience structural instability during static relaxation, which is not common in FCC HEAs [15,16]. Contrary to sluggish diffusion, the wide distribution of vacancy migration energy can lead to preferential migration through low-barrier sites, promoting vacancy diffusion [15]. In addition, based on the simulation of defect accumulation, isolated point defects and small defect clusters are preferred at both room and high temperature in VTaW and VTaTi [25]. In contrast, large defects were observed from the interatomic potential of average atom model, suggesting that the energy inhomogeneity of defects including both point defects and defect clusters has a significant impact on defect clustering.

Small vacancy clusters are an essential building block for large vacancy microstructure formation and play a significant role in defect generation, annihilation and evolution. Compared to small interstitial clusters, small vacancy clusters are less stable and can emit vacancies at reactor temperature, which can then be absorbed by various types of defect sinks including voids. In BCC metals, divacancy and trivacancy are mostly mobile and can migrate over long distances, whereas larger clusters tend to have reduced mobility [26,27]. Since the migration of tetravacancy requires dissociation, it is generally considered as the first possible stable nucleus for vacancy clustering [28]. Currently, a systematic first-principles calculation of small vacancy clusters is lacking in both FCC and BCC HEAs. It is of great scientific interest to explore how the local lattice distortion impacts their stability and clustering tendency under irradiation.

In this work, NbZrTi-based HEA $Nb_{0.75}ZrTiV_{0.5}$ was studied due to the promising mechanical performance of this group of materials [11,29,30]. The NbZrTiV alloy has been shown to have good ductility and tensile properties [31–34], as well as other favorable properties for nuclear applications [35]. Two different elemental ordering structures were investigated: random solid solution (RSS) and short-range order (SRO), as both could be present in HEAs [36–38]. The SRO structure has been shown to have a large influence on the defect diffusion [39,40] and can also be promoted during the period of irradiation [41]. Small vacancy clusters of divacancy, trivacancy and tetravacancy were simulated at different positions with the first-principles method. The energies and stable cluster configurations were analyzed. The classical MD simulations were also performed to study the impact of the energetics of small vacancy clusters on their diffusion behavior at high temperature.

2. Method

First-principles calculations were performed with the Vienna ab initio simulation package (VASP) based on the density functional theory (DFT) and the projector augmented wave (PAW) method [42]. The generalized gradient approximation (GGA)

Table 1
Number of vacancy configurations simulated in the RSS and SRO structure.

Configuration	RSS structure	SRO structure
v_1	95	95
$v_2(2)$	60	60
$v_2(1)$	20	/
$v_2(3)$	20	/
$v_3(112)$	60	60
$v_3(124)$	20	/
$v_3(223)$	20	/
$v_4(111122)$	60	60
$v_4(111223)$	30	/
$v_4(111224)$	30	/

with the Perdew–Burke–Ernzerhof (PBE) exchange-correlation parametrization was used in the calculations [43]. $Nb_{0.75}ZrTiV_{0.5}$ ($Nb_{30}Zr_{39}Ti_{39}V_{20}$), pure Nb and pure V were simulated within a 128-atom supercell of $4 \times 4 \times 4$ BCC lattice. The RSS structure and SRO structure were studied in $Nb_{0.75}ZrTiV_{0.5}$. The RSS structure was created by the special quasi-random structure (SQS) method by assuring the quasi-random appearance probabilities of each element in the first nearest neighbor (1 NN) and 2 NN with the Alloy Theoretic Automated Toolkit [44–46]. The SRO structure was obtained by the DFT + Monte Carlo method at a temperature of 500 K. The atom positions were swapped according to the acceptance criterion of Metropolis-Hastings sampling to generate a SRO structure that is energetically more stable than the RSS structure [15,47]. Gamma-centered k-point meshes of $2 \times 2 \times 2$ and $3 \times 3 \times 3$ were used for $Nb_{0.75}ZrTiV_{0.5}$ and pure metals, respectively. The use of coarse k-point sampling in HEA is a compromise between the accuracy of a single calculation and the large number of cases required for sampling the variations induced by the complexity of chemical environment. The cutoff energy of the plane-wave basis was 400 eV. The force criterion for ionic steps was set to 0.01 eV/Å and the energy criterion for electronic self-consistency step was set to 10^{-4} eV.

Different structures of monovacancy, divacancy, trivacancy and tetravacancy were simulated within a fixed volume. The monovacancy was sampled at 25 lattice sites for Nb, Zr and Ti vacancy and all 20 lattice sites for V vacancy. For vacancy clusters, there exists different configurations, as shown in Fig. 1. The cluster notation is based on the pair separation distances among different vacancy sites in unit of nearest neighbor [48]. For instance, $v_3(112)$ is the most compact trivacancy configuration in which vacancies are separated by distances of 1 NN, 1 NN and 2 NN. The number of simulated cases for each configuration is listed in Table 1. The most energetically favorable configurations in pure Nb and V, which correspond to $v_2(2)$, $v_3(112)$ and $v_4(111122)$, were simulated in both RSS and SRO structure. In addition, metastable vacancy cluster configurations based on the energy of pure Nb and V were also simulated including $v_2(1)$, $v_2(3)$, $v_3(124)$, $v_3(223)$, $v_4(111223)$ and $v_4(111224)$. In total, 690 different configurations of monovacancy and vacancy cluster were simulated.

The formation energy of monovacancy or vacancy clusters ($E_{v_n}^f$) was calculated by:

$$E_{v_n}^f = E_{v_n} + \sum_{i=1}^{4} k_i \mu_i - E_{per},$$ (1)

where E_{v_n} is the total energy of the n-vacancy structure, k_i is the number of element type i removed from the system, μ_i is the chemical potential of element type i, and E_{per} is the total energy of the perfect lattice. The elemental chemical potential was calculated by the Widom-type substitution approach based on 24 sets of structures with atom substitution [18,49]. The binding energy of
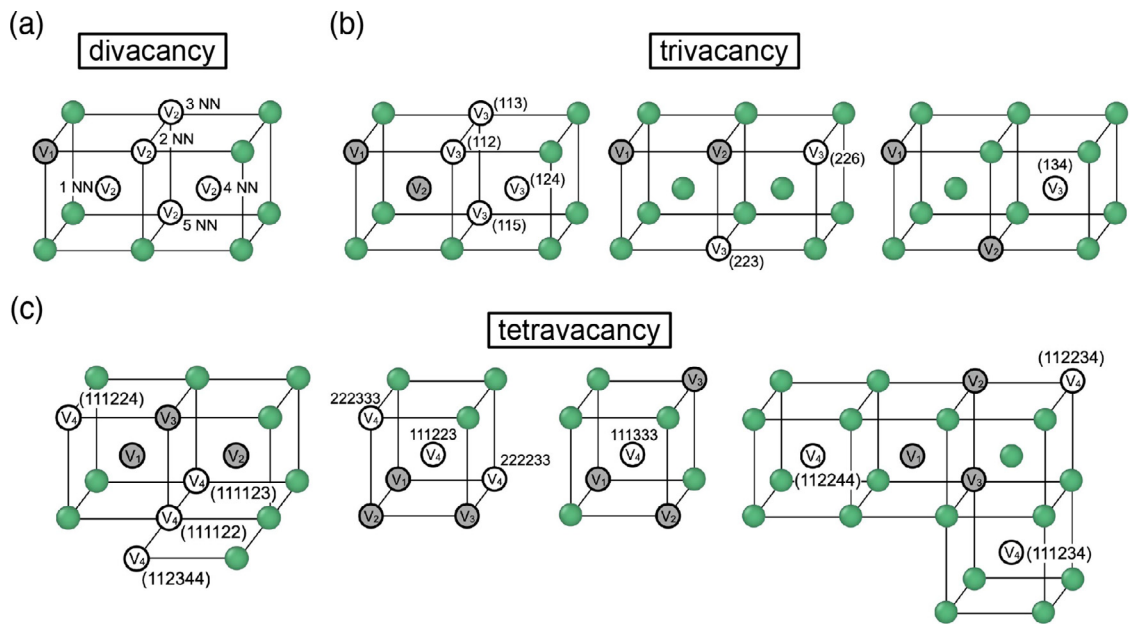
Fig. 1. Different configurations of divacancy, trivacancy and tetravacancy clusters. V_i represents the ith vacancy site in the vacancy cluster. The cluster notation is based on the neighboring distances among different pairs of vacancy sites [48].

vacancy clusters ($E_{v_n}^b$) was determined by:

$$E_{v_n}^b = \sum_{i=1}^{4} k_i \overline{E}_{v_1,i} - E_{v_n} - (n-1) \times E_{per}, \qquad (2)$$

where $\overline{E}_{v_1,i}$ corresponds to the expected system energy with a monovacancy of element type i. In this study, the $\overline{E}_{v_1,i}$ was determined by the average value of the corresponding cases and it was reasoned that during the diffusion of vacancy cluster, its stability depends on the energy states of monovacancies around the vacancy cluster, which can have a wide range of energies. Eq. (2) is also equivalent to:

$$E_{v_n}^b = \sum_{i=1}^{4} k_i \overline{E}_{v_1,i}^f - E_{v_n}^f. \qquad (3)$$

Here, the calculated binding energy is relative to a set of independent monovacancies [48,50,51]. The Wigner–Seitz surface area (S_{WS}) of different vacancy cluster configurations was determined by Voronoi tessellation based on an unrelaxed BCC lattice and was normalized by the square of lattice constant (S_{WS}/a_0^2) for comparison among different materials [52].

The classical MD simulations of vacancy cluster diffusion were performed with the LAMMPS code. The embedded atom method (EAM) potential was employed using the alloy model from Ref. [53] and the embedding function from Ref. [54]. The potential parameters of Nb and V were taken from Ref. [55] and Ref. [25], respectively, and those of Zr and Ti were taken from Zhou et al. [56]. The vacancy formation energy was included in the potential fitting and this form of potential has been successfully used to model the radiation defect accumulation in BCC MPEA [25]. The vacancy diffusion was simulated for divacancy, trivacancy and tetravacancy in pure Nb, pure V, RSS $Nb_{0.75}ZrTiV_{0.5}$ and SRO $Nb_{0.75}ZrTiV_{0.5}$. The simulation box consisted of a $20 \times 20 \times 20$ BCC supercell with periodic boundary conditions. The SRO structure was constructed by the hybrid Monte Carlo and MD method under canonical ensemble at 500 K. The SRO tendency of different atom pairs is consistent with the first-principles calculations. The diffusion of different materials was compared at an absolute temperature of 700 K and an homologous temperature (T/T_m) of 0.32, which corresponds
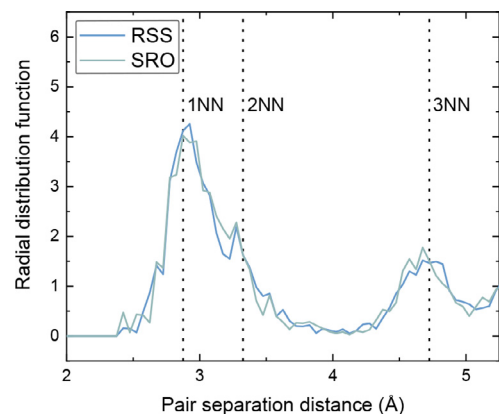

Fig. 2. Radial distribution function of random solid solution and short-range order structure in $Nb_{0.75}ZrTiV_{0.5}$.

to 980 K, 583 K and 700 K in Nb, V and $Nb_{0.75}ZrTiV_{0.5}$, respectively. The melting temperature (T_m) was determined by the solid-liquid coexistence method [57]. The most compact vacancy configurations were used as initial structures. The NVT ensemble with Nosé–Hoover thermostat was used with a timestep of 1 fs for a total simulation time of 10 ns. For each type of vacancy cluster, 10 and 15 cases were simulated at each temperature for the pure metals and the HEA structures, respectively.

3. Results

3.1. Structural properties of perfect lattice

Based on the first-principles calculations, the lattice parameter of the RSS structure is 3.334 Å. The radial distribution function of the optimized RSS structure is shown in Fig. 2, where large local lattice distortion can be observed. We note that although there is a large overlap between the 1 NN and 2 NN peak, the studied structure still has different peaks in the radial distribution function corresponding to different neighboring shells, unlike liquid having continuum at long range [58,59]. The average atomic dis-
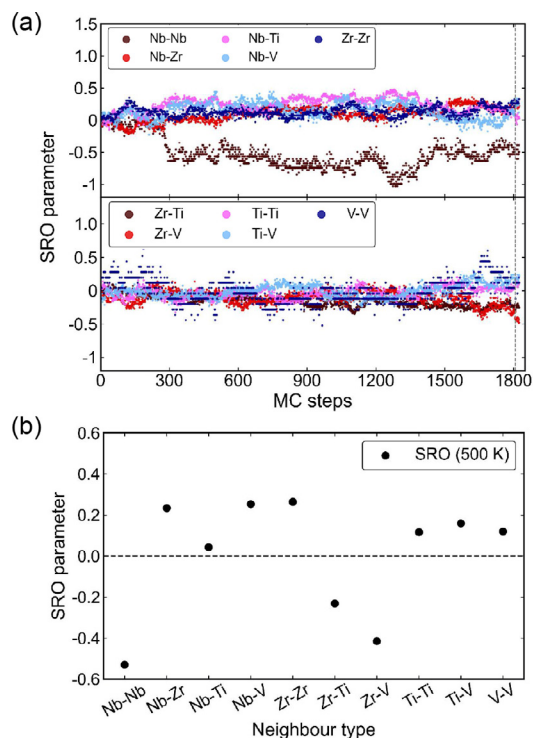
Fig. 3. (a) Evolution of 1 NN SRO parameter with Monte Carlo steps. The vertical dashed line shows the Monte Carlo step selected for vacancy simulations. (b) Final SRO parameters for different neighbor types in the SRO structure.

Fig. 4. Formation energy distribution of monovacancy in the RSS structure.

placement compared to the unrelaxed lattice is 0.217 Å, which is relatively large among different BCC MPEAs [15,16,23]. For comparison, the average displacement normalized to the lattice constant is 6.5%, which is larger than 2.8% from VTaCrW [16] and 5.1% from NbZrTi [15].

For the SRO structure, the evolution of 1 NN Warren-Cowley SRO parameters [47,60] with Monte Carlo steps is shown in Fig. 3(a). SRO parameters of zero correspond to a perfect RSS structure. Negative SRO parameters indicate preferential clustering of the corresponding atom pairs, whereas positive SRO parameters correspond to the opposite. The system energy starts to stabilize from ~600 Monte Carlo steps. The SRO structure used for vacancy simulations is selected at ~1800 Monte Carlo steps. It can be seen that in the selected SRO structure, the most pronounced clustering comes from Nb-Nb, followed by Zr-V and Zr-Ti (see Fig. 3(b)). Most atom pairs fluctuate around a SRO parameter of zero with no significant clustering preference except for Nb-Nb. The lattice parameter is 3.336 Å in the SRO structure and the energy per atom is ~32 meV lower than the RSS structure. The local lattice distortion is comparable to that of RSS structure (see Fig. 2).

3.2. Vacancy properties in random solid solution structure

According to the first-principles calculations, the monovacancy in the RSS structure exhibits a wide energy distribution, as shown in Fig. 4. The average formation energies for Nb, Zr, Ti and V are 0.95 eV ± 0.57 eV, 0.93 eV ± 0.61 eV, 1.00 eV ± 0.55 eV and 1.23 eV ± 0.49 eV, respectively. The V vacancy has a slightly higher formation energy than the other three elements. The large variation in the energy distribution is induced by the difference in chemical environment and local lattice distortion in the vacancy neighborhood. The relative positions of different types of elements around the vacancy can result in different formation energies at different sites. In addition, vacancy-atom exchange can occur during structural optimization, which further reduces the vacancy for-
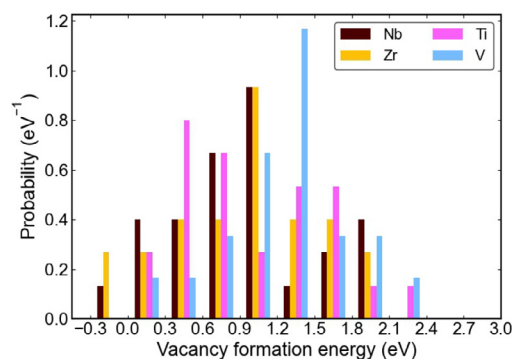
mation energy at certain sites and increases the energy variation [15]. With this large energy variation, vacancies with low formation energy have a much higher probability to exist at thermal equilibrium [61]. Compared to 2.77 eV in pure Nb and 2.07 eV in pure V, the monovacancy formation energy is much lower in the studied structure.

Three different divacancy structures were simulated: $v_2(1)$, $v_2(2)$ and $v_2(3)$, which correspond to divacancies with vacancy distances of 1 NN, 2 NN and 3 NN, respectively (see description of cluster notation in Section 2). The $v_2(2)$ is the most stable configuration in pure Nb and V with the lowest formation energy [50,62]. Fig. 5(a) and (b) show the formation and binding energy of divacancy in the RSS structure for different final divacancy configurations. The final configuration can differ from the initial one because neighboring atoms can move into the initial vacancy site during static structural optimization. The corresponding fraction of configuration change is listed in Fig. 5(c). The fractions of final configurations for each initial configuration are also shown in figures of formation and binding energy by using markers of different sizes. It is shown that $v_2(1)$ is mostly unstable, and it has a high probability to transform to $v_2(2)$ and $v_2(3)$ by one exchange between vacancy and 1 NN and to $v_2(4)$ by two exchanges. The $v_2(2)$ configuration remains to be $v_2(2)$ in 48% of the cases. It can barely change to $v_2(1)$ but has a 41% probability to relax to $v_2(4)$. The change to these two configurations both involve only one atom replacement from one of the four 1 NN atoms, suggesting a strong preference to adopt the $v_2(4)$ structure from $v_2(2)$. The $v_2(3)$ configuration has a 50% probability to be stable and also prefers to form loose vacancy configurations. The formation of $v_2(2)$ from $v_2(3)$ requires two vacancy-atom exchanges, which explains the lower probability of this relaxation pathway. Based on these structural changes, it can be seen that the occurrence probability of final vacancy configurations depends on the initial configurations and less compact vacancy configurations are favored.

In $Nb_{0.75}ZrTiV_{0.5}$, the divacancy formation energy is much lower than Nb and V (see Fig. 5(a)). Besides the energy preference for $v_2(2)$ in some cases, the formation energy of $v_2(4)$ and beyond tends to be lower than more compact configurations. For instance, with an initial configuration of $v_2(2)$, the formation energies for final configurations of $v_2(2)$ and $v_2(4)$ are 2.29 eV ± 0.67 eV and 1.23 eV ± 1.00 eV, respectively. The binding energy also exhibits the consistent trend, showing higher binding energy for loose divacancy structures (see Fig. 5(b)). A negative binding energy indicates that the divacancy is energetically less stable than two monovacancies that are farther apart, whereas a positive binding energy implies attractive force for cluster formation. Although large energy variation is present due to the variation of local chemical environment, a positive binding energy was observed in $v_2(4)$ and beyond. In comparison, the binding energy of $v_2(2)$ is on average lower than that of V and Nb and has
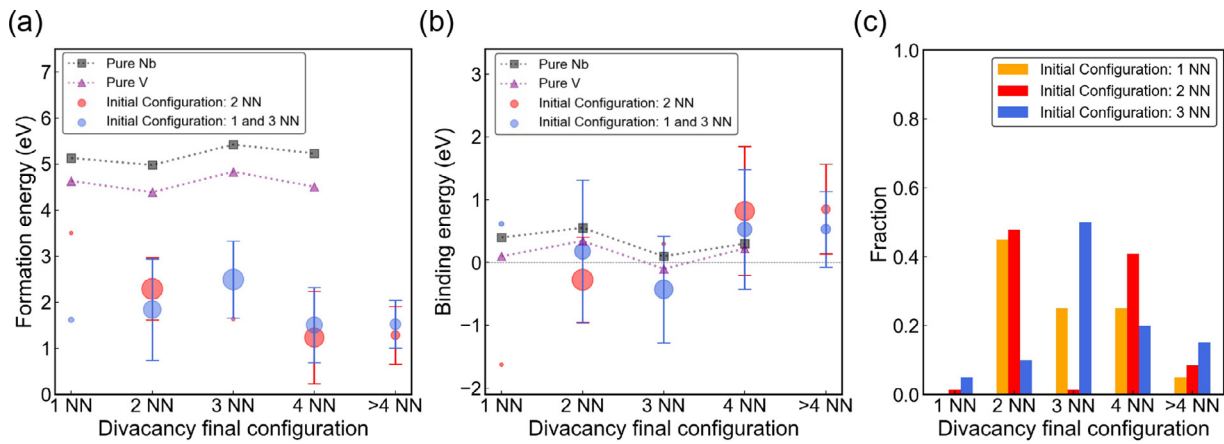
Fig. 5. Divacancy energetics in the RSS structure: (a) divacancy formation energy, (b) divacancy binding energy, (c) fraction of final configurations for different initial configurations. The marker areas in (a) and (b) are proportional to the percentage of cases for each initial configuration. The error bars are shown for more than 3 cases.
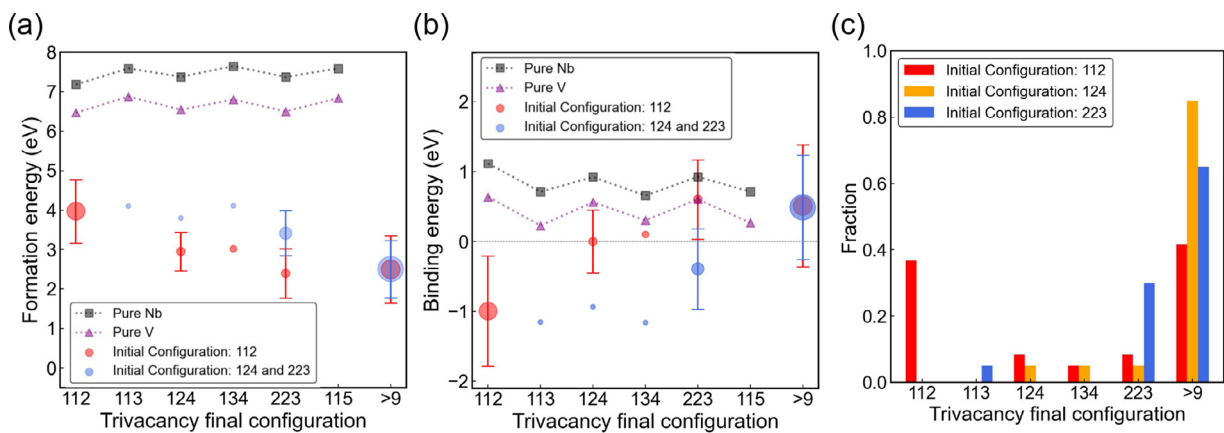

Fig. 6. Trivacancy energetics in the RSS structure: (a) trivacancy formation energy, (b) trivacancy binding energy, (c) fraction of final configurations for different initial configurations. The marker areas in (a) and (b) are proportional to the percentage of cases for each initial configuration. The error bars are shown for more than 3 cases.

a large portion of its distribution extending into negative region, indicating its less likelihood of formation from an energy perspective.

Trivacancy structures of $v_3(112)$, $v_2(124)$ and $v_2(223)$ were simulated. The $v_3(112)$ has the lowest formation energy in pure Nb and V. As shown in Fig. 6, a large fraction of the initial structures are unstable and stabilize to less compact configurations. The stable fractions for $v_3(112)$, $v_2(124)$ and $v_2(223)$ are 37%, 5.0% and 30%, respectively (see Fig. 6(c)). 55% of the structures change to loose configurations that have an average distance among vacancies larger than 3 NN ($v_3(>9)$), such as $v_2(145)$, $v_2(235)$, $v_2(247)$, etc. The possible final configurations are numerous and the distance between vacancies can be as far as 8 NN – 13 NN. Considering the supercell size of $4 \times 4 \times 4$, such situation is close to the formation of weakly interacting monovacancies. If we assume only one vacancy-atom exchange with 1 NN with the same probability in all directions, for initial configurations of $v_2(124)$ and $v_2(223)$, the unstable fractions of final configurations with $v_3(\leq 9)$ should be 52%. However, the corresponding fraction is much smaller, showing a preference for loose configurations. The trivacancy formation energy in $Nb_{0.75}ZrTiV_{0.5}$ is much smaller than Nb and V (see Fig. 6(a)). There is a tendency of decreasing formation energy with increasing vacancy distance. The formation energy is 3.97 eV $\pm$ 0.80 eV for the most tightly bound final configuration of $v_3(112)$ and lowers to 2.50 eV $\pm$ 0.79 eV for final configurations of $v_3(>9)$. The binding energy is negative for a large fraction of $v_3(112)$ final configurations and grad-

ually increases to positive energies in less compact configurations (see Fig. 6(b)).

The most stable tetravacancy configuration of $v_4(111122)$ in Nb and V and two metastable tetravacancy configuration of $v_4(111223)$ and $v_4(111224)$ were studied with the corresponding results shown in Fig. 7. There are more possible configurations with the increase of the number of vacancies. Most cases involve large structural adjustment with replacement of vacancy sites from multiple atoms during the relaxation process. The trend is similar with those of divacancy and trivacancy, showing a tendency of vacancies moving apart and decreasing in formation energy with increasing distances among vacancies. The difference in energy among compact and loose configurations tends to be more pronounced for tetravacancy. For instance, the most compact $v_4(111122)$ configuration has mostly negative binding energies, whereas tetravacancies with an average vacancy distance equal to or larger than 4 NN ($v_4(>15)$) have mostly positive binding energies.

3.3. Vacancy properties in short-range order structure

In the SRO structure, the average monovacancy formation energies for Nb, Zr, Ti and V are 1.70 eV $\pm$ 0.40 eV, 2.04 eV $\pm$ 0.44 eV, 1.53 eV $\pm$ 0.31 eV and 1.27 eV $\pm$ 0.32 eV, respectively (see Fig. 8). Compared to the RSS structure (see Section 3.2), the monovacancy formation energy is much higher with a significant reduction in low-energy states that lie below ~ 1.0 eV. No noticeable
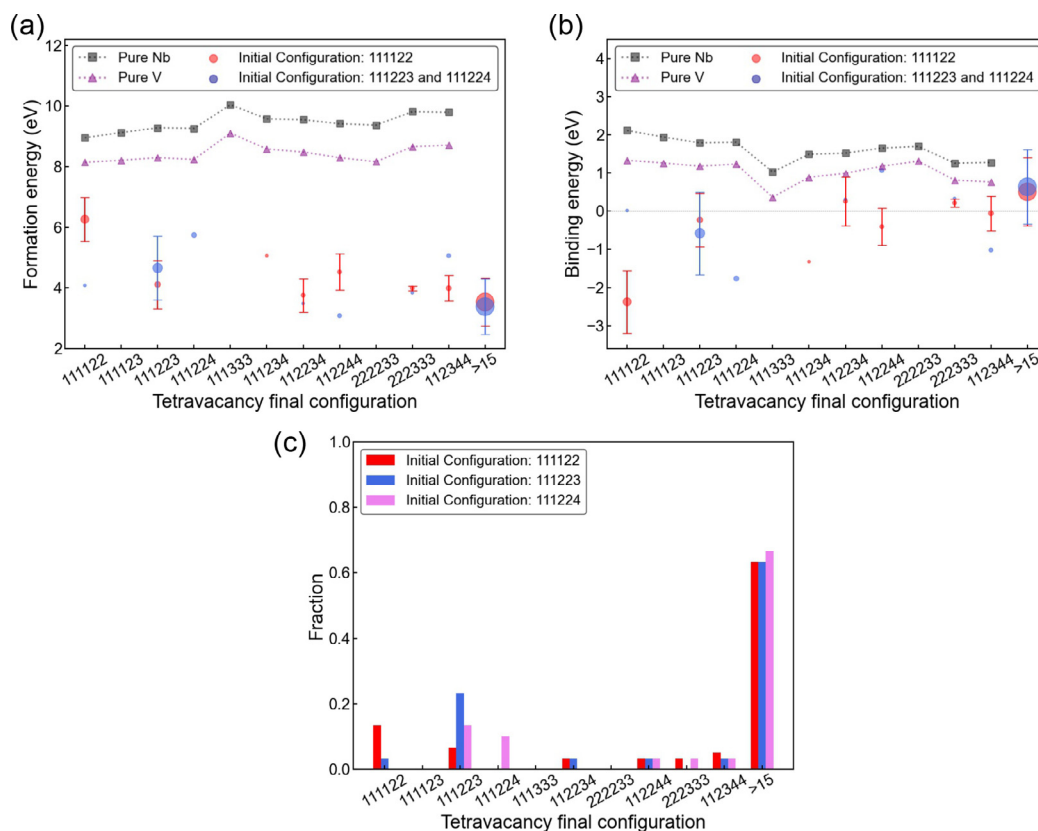
Fig. 7. Tetravacancy energetics in the RSS structure: (a) tetravacancy formation energy, (b) tetravacancy binding energy, (c) fraction of final configurations for different initial configurations. The marker areas in (a) and (b) are proportional to the percentage of cases for each initial configuration. The error bars are shown for more than 3 cases.

change was observed in the vacancy formation energy of V. However, the monovacancy formation energies of Nb, Zr and Ti increase significantly. The SRO structure is energetically more stable than the RSS structure. Therefore, the energy reduction induced by vacancy structural relaxation is smaller accordingly. The fractions of structures that undergo vacancy-atom exchange are 39% and 16% in the RSS and SRO structure, respectively, implying the higher stability of initial vacancy configurations in the SRO structure.

Vacancy cluster configurations of $v_2(2)$, $v_3(112)$ and $v_4(111122)$ were studied in the SRO structure and the corresponding results are presented in Figs. 9–11, respectively. Compared to the RSS structure (see Section 3.2), these configurations are more stable in the SRO structure. The stable fractions of $v_2(2)$, $v_3(112)$ and $v_4(111122)$ configurations are 83.3%, 70.0% and 51.7%, respectively. The rest of the configurations can still undergo vacancy-atom ex-

changes and stabilize to less compact configurations. The formation energies of vacancy clusters are lower than those of pure Nb and V but higher than those of RSS structure. For the tightly bound final configurations of $v_2(2)$, $v_3(112)$ and $v_4(111,122)$, the SRO structure has average formation energies of 3.19 eV $\pm$ 0.60 eV, 4.95 eV $\pm$ 0.59 eV and 6.71 eV $\pm$ 0.62 eV, respectively, and the RSS structure has average formation energies of 2.29 eV $\pm$ 0.67 eV, 3.97 eV $\pm$ 0.80 eV and 6.26 eV $\pm$ 0.73 eV, respectively. For the loose final configurations of $v_2(4)$, $v_3(>9)$ and $v_4(>15)$, the SRO structure has average formation energies of 2.59 eV $\pm$ 0.43 eV, 3.87 eV $\pm$ 0.64 eV and 5.79 eV $\pm$ 0.54 eV, respectively, and the RSS structure has average formation energies of 1.23 eV $\pm$ 1.00 eV, 2.50 eV $\pm$ 0.71 eV and 3.54 eV $\pm$ 0.79 eV, respectively. It is also found that for vacancy clusters with high formation energy, the neighboring environment tends to be enriched in Nb, whereas the opposite is true for cases with low formation energy. The binding energy also increases with increasing vacancy distances in the SRO structure. One difference from RSS structure is that the compact configurations have on average small positive binding energies in the SRO structure. However, the less compact configurations still have higher binding energies, indicating the role of spontaneous vacancy-atom exchange in lowering the system energy.

3.4. Diffusion at high temperature with classical MD simulations

The impact of vacancy cluster binding energy on the diffusion stability was studied for V, Nb, RSS $Nb_{0.75}ZrTiV_{0.5}$ and SRO $Nb_{0.75}ZrTiV_{0.5}$ by classical MD simulations. In the studied HEA, the instability of compact cluster configurations was also seen during static structural optimization and there is a general trend of decreasing formation energy with increasing distances among va-
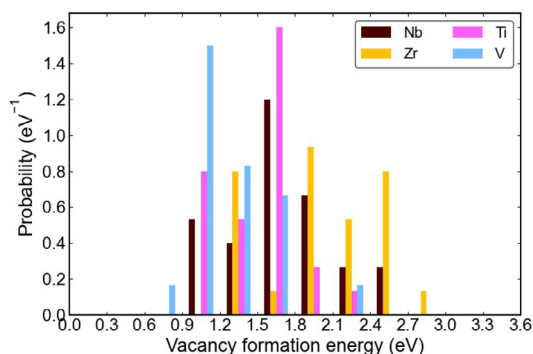

Fig. 8. Formation energy distribution of monovacancy in the SRO structure.
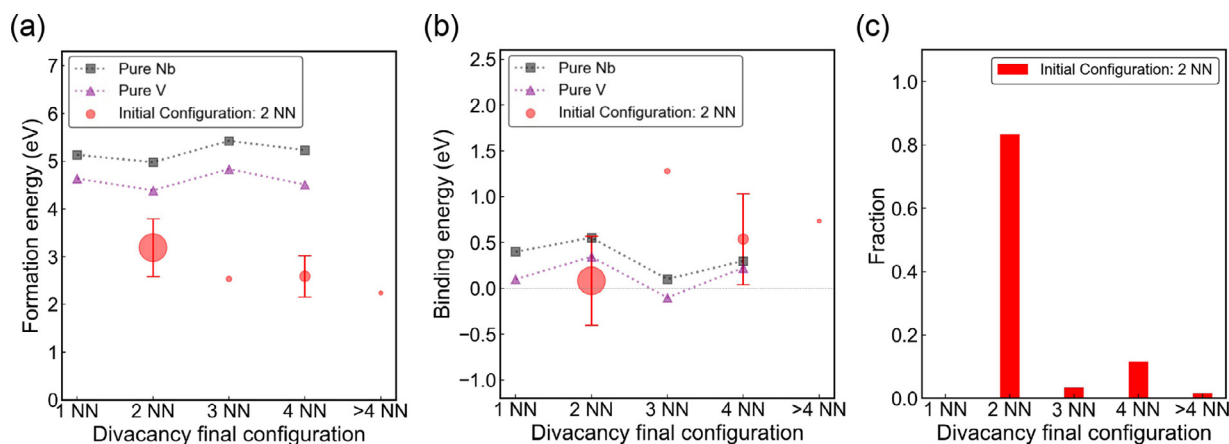
Fig. 9. Divacancy energetics in the SRO structure: (a) divacancy formation energy, (b) divacancy binding energy, (c) fraction of final configurations from the same initial configuration. The marker areas in (a) and (b) are proportional to the percentage of cases. The error bars are shown for more than 3 cases.

Fig. 10. Trivacancy energetics in the SRO structure: (a) trivacancy formation energy, (b) trivacancy binding energy, (c) fraction of final configurations from the same initial configuration. The marker areas in (a) and (b) are proportional to the percentage of cases. The error bars are shown for more than 3 cases.
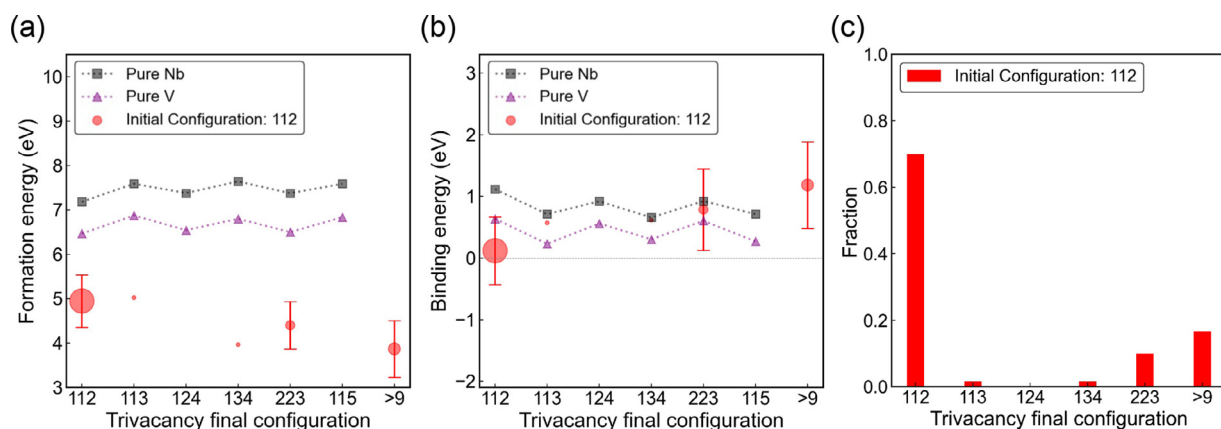
cancies in the cluster, which is consistent with the first-principles results. Due to the difference in melting temperature among different materials, the diffusion simulations were performed both at the same absolute temperature of 700 K and the same homologous temperature (T/T_m) of 0.32 (700 K for $Nb_{0.75}ZrTiV_{0.5}$). The time fraction of cluster dissociation and the average cluster size during a 10-ns diffusion period were determined, as presented in Fig. 12. A cluster was considered to be dissociated when the distance among vacancies was larger than a cutoff distance of 6 Å. The average cluster size was calculated based on the maximum cluster size at each moment. At 700 K, vacancy clusters in Nb barely dissociate due to the higher binding energy and the higher melting temperature. Although V has a lower melting temperature (TT_m: 1810 K) than $Nb_{0.75}ZrTiV_{0.5}$ (T_m: 2200 K), the later still has a higher probability of dissociation. Accordingly, the studied HEA has the lowest average cluster size among the studied materials. At the same homologous temperature of 0.32, V has an extremely low probability of dissociation due to the lower temperature. Although the corresponding absolute temperature in Nb is higher, it is still more stable than the studied HEA. The most prominent difference between pure metals and the studied HEA was observed in the case of tetravacancy. It is known that small vacancy clusters are generally unstable at high temperature. The cluster binding energies in Nb and V increase with the cluster size (see Figs. 5–7), resulting in increasing cluster stability. For V at 700 K and Nb at 980 K, the thermal driving force is sufficient to lead to a relatively high dissociation probability for divacancy and trivacancy but

not for tetravacancy within the time frame of the simulation. In contrast, due to the low binding energy of the studied HEA for all three types of vacancy clusters including tetravacancy, the dissociation probability remains high.

Based on MD simulations, the RSS and SRO structure have similar dissociation probability. Although being considered as one cluster, less compact configurations were more frequently seen in both RSS and SRO structures compared to pure metals, which is also consistent with the results from first-principles calculations. There is also another important effect taking place during the diffusion. In the SRO structure, cluster diffusion tends to be localized in Nb-depleted and Ti-rich regions based on the analysis of the elemental fraction in the 1 NN and 2 NN of vacancy clusters. By examining the cluster diffusion trajectories, it is found that vacancy clusters are frequently trapped in such confined SRO region in form of loose cluster configurations. For pure metals, once the cluster is dissociated, it is more likely for vacancies to be distributed farther away from each other. There comparisons show that small vacancy clusters in $Nb_{0.75}ZrTiV_{0.5}$ have lower stability than its constituent elements, which affects the nucleation of void embryo.

4. Analysis and discussion

In many BCC metals, compact vacancy clusters with spherical or quasi-spherical shape are generally preferred [52,63,64]. For the smallest cluster of v_2, either $v_2(1)$ or $v_2(2)$ configuration can be energetically favorable. For instance, W and Mo have a lower
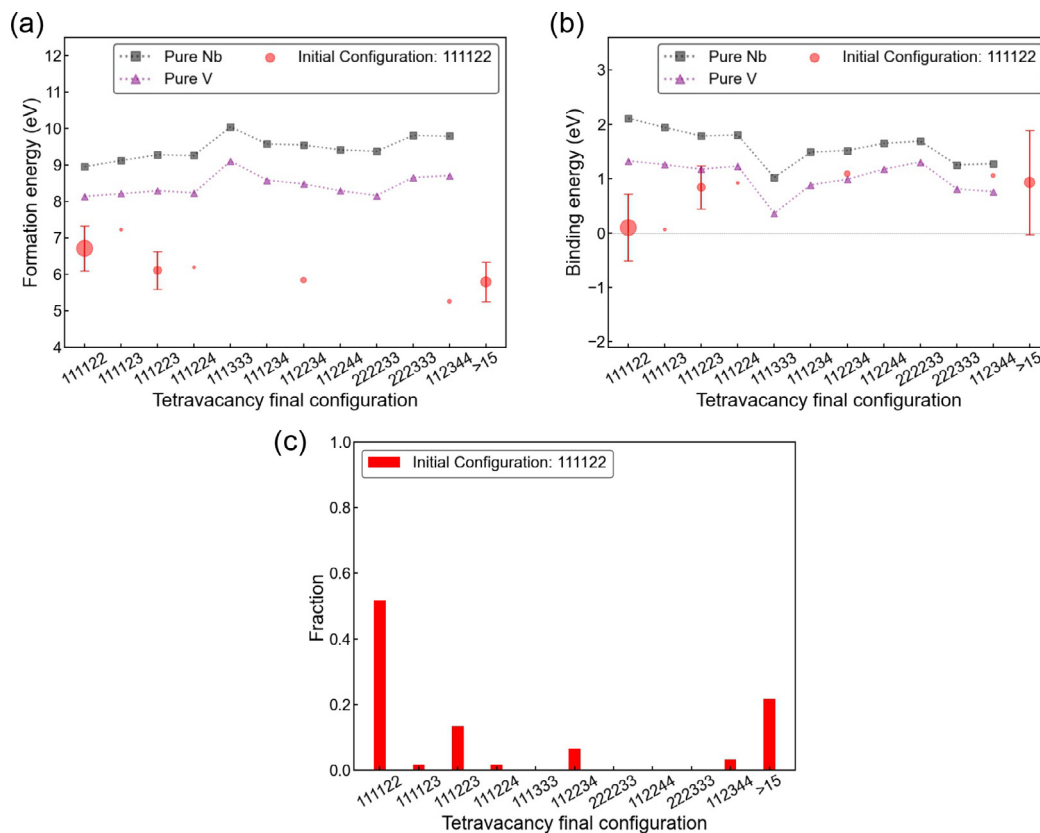
Fig. 11. Tetravacancy energetics in the SRO structure: (a) tetravacancy formation energy, (b) tetravacancy binding energy, (c) fraction of final configurations from the same initial configuration. The marker areas in (a) and (b) are proportional to the percentage of cases. The error bars are shown for more than 3 cases.
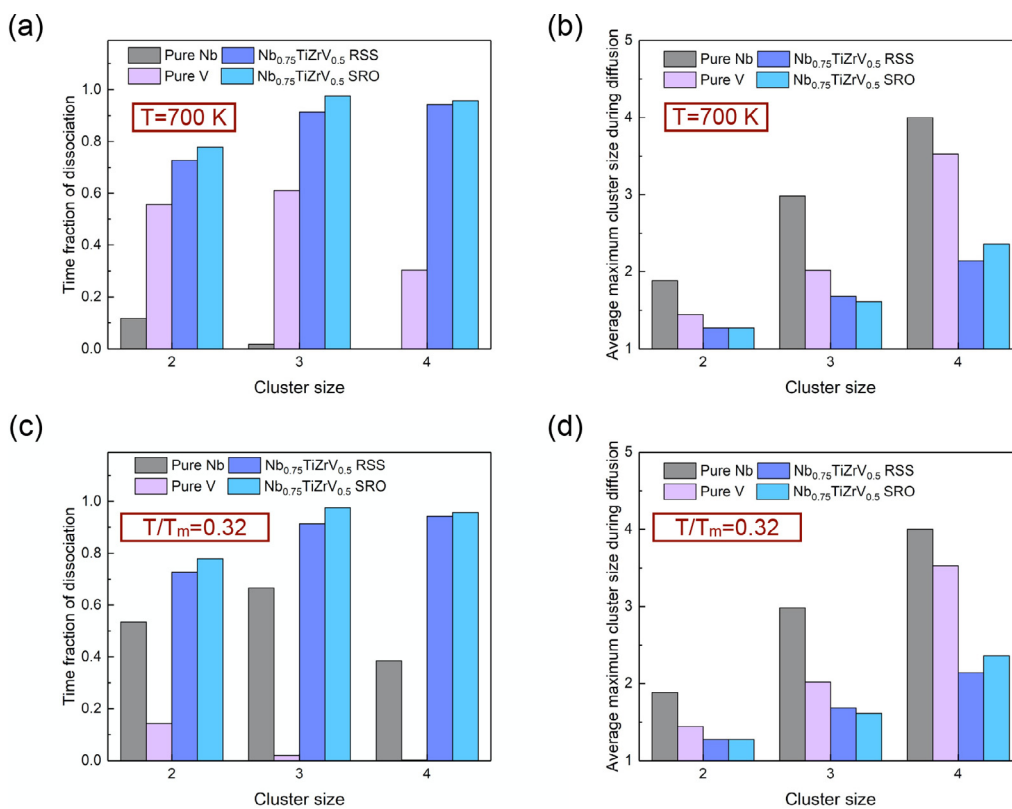

Fig. 12. (a) The time fraction of vacancy cluster dissociation and (b) average cluster size during 10-ns diffusion at 700 K. (c) The time fraction of vacancy cluster dissociation and (d) average cluster size during 10-ns diffusion at a T/T_m of 0.32, which corresponds to 980 K, 583 K and 700 K in Nb, V and $Nb_{0.75}ZrTiV_{0.5}$, respectively.
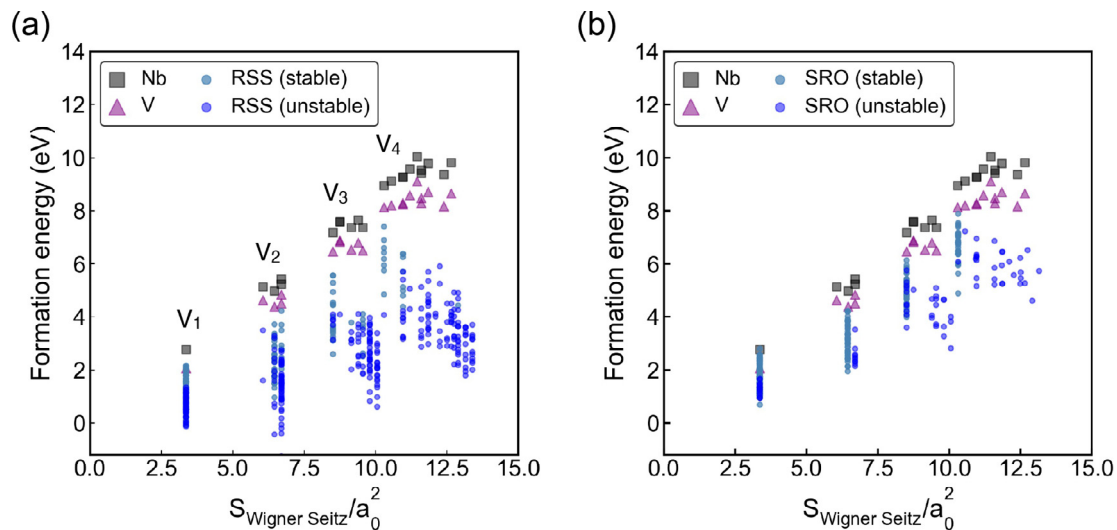
Fig. 13. Formation energies of ν_1 to ν_4 as a function of the normalized Wigner–Seitz vacancy surface area in the (a) RSS structure and (b) SRO structure. The stable and unstable initial configurations are marked in light blue and blue, respectively.

formation energy for $\nu_2(1)$, whereas Ta, Nb, V and α-Fe prefer $\nu_2(2)$ configuration [52,62]. But in general, the formation energy of vacancy clusters tends to increase with the surface area, as the formation energy is closely related to the energy cost from the surface [28]. However, as shown in Fig. 13, the vacancy formation energy in Nb$_{0.75}$ZrTiV$_{0.5}$ tends to decrease with the normalized Wigner–Seitz surface area. This is largely due to the vacancy-atom exchange in the direction of less compact configurations, which have larger surface areas. Such vacancy-atom exchange induced by structural instability is more pronounced in the RSS structure due to the higher energy state of the perfect RSS lattice. First, in the studied HEA, the severe local lattice distortion allows a higher degree of freedom for structural adjustment around the lattice sites, resulting in the overall lower formation energy. Second, vacancy sites provide potential pathways for vacancy-atom exchange and anti-sites with lower energy will be preferentially adopted. Third, vacancy-atom exchange can lead to either compact or less compact configurations. The decreasing energy with less compact configurations could be due to the reason that it can effectively relieve the internal stress from the initial vacancy configurations with more neighboring atoms taking part in the structural relaxation. Another important observation is that the energy variation for the same final vacancy configuration is large owing to the large difference in the local chemical environment. Whether a specific configuration has a lower or higher formation energy depends heavily on the local atomic arrangement. This is intrinsic to HEA due to the chemical disorder and chemical complexity. In Nb and V, the formation energy does increase with the surface area, but the magnitude of increase from the cost of surface energy is small compared to the large formation energy distribution from the HEA, implying the larger role of local energy variation over the surface area in decreasing the system energy. Thus, vacancy configurations will accommodate to the most energetically stable configuration around the local region.

As shown in Fig. 14 (a) and (b), the formation energy evolution shows a moderate negative correlation with the average atomic displacement during the vacancy structural relaxation ($\bar{d}$) in the RSS and SRO structure. The correlation is stronger in the RSS structure because large displacement induced by one or more vacancy-atom exchanges occurs more frequently in the RSS structure and such site exchange can effectively reduce the system energy. At a fixed relaxed distance, the range of formation energy is wide, indicating strong site-to-site variation. To further understand

these effects, the formation energy of unrelaxed vacancy structure ($E^{f}_{v_n,unrelaxed}$) was determined, which was calculated by using the system energy of the unrelaxed vacancy structure instead of the energy of the final configuration (E_{v_n}) in Eq. (1). In addition, an explanatory model was used to estimate the formation energy, which is defined as:

$$E^{f}_{v_n,estimate} = E^{f}_{v_n,unrelaxed} - k\bar{d}, \qquad (4)$$

where k in an adjustable constant to obtain the highest coefficient of determination between the estimated formation energy and true formation energy. It can be seen from Fig. 14(c) that the unrelaxed formation energy is initially much larger than the relaxed formation energy in the RSS structure. The energy decreases significantly by structural relaxation including vacancy-atom exchanges. In comparison, such energy decrease is smaller in the SRO structure (see Fig. 14(d)), where the initial local energy state plays a larger role in determining the true formation energy. Eq. (4) shows two important factors that influence the final vacancy energy, i.e., the initial energy state of the vacancy configuration and the extent of structural adjustment. Here, the structural adjustment is reflected by a single parameter of average atomic displacement. Exactly speaking, the atomic relaxation near the vacancy should have a higher impact and the actual physical process involves the redistribution of ionic charge and electron density, which is clearly more convoluted. Nevertheless, as presented in Fig. 14(c) and (d), the proposed model can explain the formation energy evolution with reasonable accuracy. The unrelaxed formation energy correlates positively with the true formation energy with a larger fluctuation, but a better linearity can be achieved by taking into account the atomic displacement in the estimated formation energy. For instance, sites with high unrelaxed formation energies and large relaxation distances can lead to lower formation energies; sites with high unrelaxed formation energies and lower extent of relaxation maintain at high-energy states. When comparing the estimated and true formation energy, the coefficient of determination is lower in the RSS structure because the vacancy-atom exchange also involves anti-site energy, which is not reflected in this explanatory model. When one atom fills into a neighbor vacancy site, the energy change is more complicated, leading to the larger variation shown in Fig. 14(c).

BCC MPEAs and HEAs exhibit severe local lattice distortion [23,24]. Instability of monovacancy [15] and single interstitial [16] has been reported in other BCC MPEAs, hinting that the
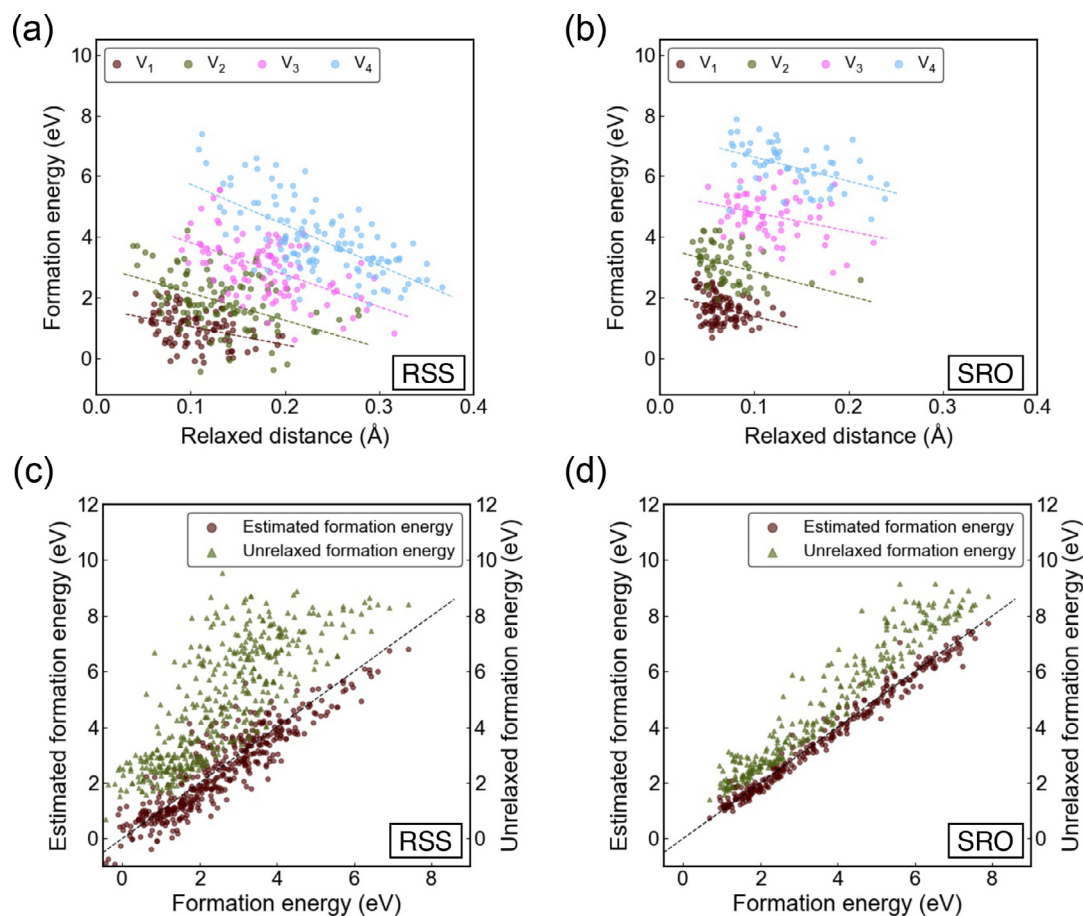
Fig. 14. (a, b) Formation energies of v_1 to v_4 as a function of the average relaxed distance per atom in the vacancy configuration in the RSS and SRO structure. (c, d) Estimated vacancy formation energy and unrelaxed vacancy formation energy in the RSS and SRO structure. The dashed lines in (c) and (d) show positions where the estimated formation energy is equal to the true formation energy.

instability of small vacancy clusters found in $Nb_{0.75}ZrTiV_{0.5}$ could be a common property among similar HEAs with large local lattice distortion. Irradiation experiment on NbZrTi showed that with heavy ion irradiation at 675 °C to a peak dose of ∼100 dpa, the formation of voids and dislocation loops in NbZrTi was significantly suppressed compared to pure Nb [15]. It was explained that low monovacancy formation energy could lead to high equilibrium vacancy concentration, which promotes thermal vacancy emission from voids and limits the void growth. Here, we showed that small vacancy clusters with compact cluster configurations have low binding energies in BCC MPEA, which could also contribute to the delayed growth of irradiation-induced voids. In the context of radiation damage, the energetics of monovacancy and small vacancy clusters has a large influence on vacancy cluster nucleation and diffusion, as well as the kinetic evolution of irradiation-induced voids [65]. During the displacement cascade induced by neutron or ion irradiation, a depleted zone with a high density of vacancies is formed in the center with interstitials located at the periphery due to replacement collisions. In this process, the stability of small vacancy clusters can affect the vacancy clustering fraction and the cluster size distribution [66,67]. More isolated vacancies and smaller vacancy clusters are expected due to the smaller binding energy of tightly bound configurations.

In the process of diffusion, as less compact configurations are favorable and different local regions have different preferences for stable cluster configurations, small vacancy clusters will have a lower probability of maintaining the same configuration by change of configurations and dissociation into smaller clusters or monova-

cancies, as evidenced from the MD simulations of vacancy cluster diffusion. In addition, cluster diffusion tends to be localized in the SRO structure, showing the impact of the spatial distribution of SRO and the potential energy inhomogeneity on cluster diffusion. In conventional BCC metals, v_3(112) can migrate without dissociation, which plays an important role in vacancy-cluster formation [48,63]. For other vacancy clusters, the migration usually involves transient dissociation into metastable configurations during vacancy jumps, such as temporary dissociation of v_4(111122) into v_1 and v_3 [48]. In the studied HEA, the behavior of diffusion, dissociation and coalescence of small vacancy clusters is expected to change due to the position- and configuration-dependent cluster stability. Future studies of vacancy clusters of larger sizes are needed to have a complete understanding of the binding energy evolution and their influence on void nucleation.

5. Conclusions

In BCC HEA $Nb_{0.75}ZrTiV_{0.5}$, the severe local lattice distortion and the variation in local chemical environment lead to a wide distribution of formation energy in monovacancy, divacancy, trivacancy and tetravacancy. The formation energies of small vacancy clusters are lower than those of pure Nb and V due to the higher extent of vacancy structural relaxation. Compared to the structure of random solid solution, the structure of short-range order has higher vacancy formation energies due to the lower energy state of the latter. During static structural optimization, the vacancy configurations can experience instability with vacancy-atom exchanges and

there is a tendency for tightly bound vacancy clusters to transform to less compact configurations. The less compact configurations have lower formation energies and higher binding energies, indicating that they are favored energetically. This is different from conventional BCC metals where minimization of surface area is generally preferred. The local vacancy formation energy of monovacancy and small vacancy clusters is dependent on the initial energy state of the vacancy structure and the magnitude of structural adjustment. The energetics of small vacancy clusters can significantly affect their diffusion process in which small vacancy clusters have a higher probability of dissociation compared to Nb and V. The distinct energy properties are expected to impact both the radiation defect generation and long-term evolution.

Declaration of Competing Interest

The authors declare that they have no known competing financial interests or personal relationships that could have appeared to influence the work reported in this paper.

Acknowledgments

References

[1] Y. Zhang, G.M. Stocks, K. Jin, C. Lu, H. Bei, B.C. Sales, L. Wang, L.K. Béland, R.E. Stoller, G.D. Samolyuk, M. Caro, W. Weber, Nat. Commun. 6 (1) (2015) 1–9.
[2] C. Lu, L. Niu, N. Chen, K. Jin, T. Yang, P. Xiu, Y. Zhang, F. Gao, H. Bei, S. Shi, M.-R. He, I.M. Robertson, W.J. Weber, L. Wang, Nat. Commun. 7 (1) (2016) 1–8.
[3] C. Lu, T. Yang, K. Jin, N. Gao, P. Xiu, Y. Zhang, F. Gao, H. Bei, W.J. Weber, K. Sun, Y. Dong, L. Wang, Acta Mater. 127 (2017) 98–107.
[4] K. Jin, C. Lu, L. Wang, J. Qu, W. Weber, Y. Zhang, H. Bei, Scr. Mater. 119 (2016) 65–70.
[5] Z. Su, T. Shi, J. Yang, H. Shen, Z. Li, S. Wang, G. Ran, C. Lu, Acta Mater. 233 (2022) 117955.
[6] Y. Zhang, Y.N. Osetsky, W.J. Weber, Chem. Rev. 122 (1) (2021) 789–829.
[7] S.J. Zinkle, J.T. Busby, Mater. Today 12 (11) (2009) 12–19.
[8] M.S. El-Genk, J.-M. Tournier, J. Nucl. Mater. 340 (1) (2005) 93–112.
[9] P. Yvon, F. Carré, J. Nucl. Mater. 385 (2) (2009) 217–222.
[10] T. Shi, P.-H. Lei, X. Yan, J. Li, Y.-D. Zhou, Y.-P. Wang, Z.-X. Su, Y.-K. Dou, X.-F. He, D. Yun, W. Yang, C.-Y. Lu, Tungsten 3 (2) (2021) 197–217.
[11] O.N. Senkov, D.B. Miracle, K.J. Chaput, J.-P. Couzinie, J. Mater. Res. 33 (19) (2018) 3092–3128.
[12] E.P. George, W. Curtin, C.C. Tasan, Acta Mater. 188 (2020) 435–474.
[13] O. El-Atwani, N. Li, M. Li, A. Devaraj, J. Baldwin, M.M. Schneider, D. Sobieraj, J.S. Wróbel, D. Nguyen-Manh, S.A. Maloy, E. Martinez, Sci. Adv. 5 (3) (2019) eaav2002.
[14] S. Chang, K.-K. Tseng, T.-Y. Yang, D.-S. Chao, J.-W. Yeh, J.-H. Liang, Mater. Lett. 272 (2020) 127832.
[15] T. Shi, Z. Su, J. Li, C. Liu, J. Yang, X. He, D. Yun, Q. Peng, C. Lu, Acta Mater. 229 (2022) 117806.
[16] S. Zhao, J. Mater. Sci. Technol. 44 (2020) 133–139.
[17] Q. Liu, S. Xia, Y. Su, J. Huang, S. Zhao, F. Luo, H. Liu, W. Ge, J. Xue, C. Wang, Y. Wang, Materialia 20 (2021) 101234.
[18] S. Zhao, G.M. Stocks, Y. Zhang, Phys. Chem. Chem. Phys. 18 (34) (2016) 24043–24056.
[19] S. Zhao, Y. Osetsky, Y. Zhang, Acta Mater. 128 (2017) 391–399.
[20] Y.N. Osetsky, L.K. Béland, A.V. Barashev, Y. Zhang, Curr. Opin. Solid State Mater. Sci. 22 (3) (2018) 65–74.
[21] Y. Osetsky, A.V. Barashev, L.K. Béland, Z. Yao, K. Ferasat, Y. Zhang, Npj Comput. Mater. 6 (1) (2020) 1–8.
[22] K. Jin, W. Guo, C. Lu, M.W. Ullah, Y. Zhang, W.J. Weber, L. Wang, J.D. Poplawsky, H. Bei, Acta Mater. 121 (2016) 365–373.
[23] H. Song, F. Tian, Q.-M. Hu, L. Vitos, Y. Wang, J. Shen, N. Chen, Phys. Rev. Mater. 1 (2) (2017) 023404.
[24] Z. Wang, W. Qiu, Y. Yang, C. Liu, Intermetallics 64 (2015) 63–69.
[25] S. Zhao, Y. Xiong, S. Ma, J. Zhang, B. Xu, J.-J. Kai, Acta Mater. 219 (2021) 117233.
[26] Y. Fan, A. Kushima, S. Yip, B. Yildiz, Phys. Rev. Lett. 106 (12) (2011) 125501.
[27] C.-C. Fu, J.D. Torre, F. Willaime, J.-L. Bocquet, A. Barbu, Nat. Mater. 4 (1) (2005) 68–74.
[28] G.S. Was, Fundamentals of Radiation Materials Science: Metals and Alloys, Springer, 2016.
[29] Z. Lei, X. Liu, Y. Wu, H. Wang, S. Jiang, S. Wang, X. Hui, Y. Wu, B. Gault, P. Kontis, D. Raabe, L. Gu, Q. Zhang, H. CHen, H. Wang, J. Liu, K. An, Q. Zeng, T.-G. Nieh, Z. Lu, Nature 563 (7732) (2018) 546–550.
[30] O. Senkov, S. Rao, K. Chaput, C. Woodward, Acta Mater. 151 (2018) 201–215.
[31] O.N. Senkov, S.V. Senkova, C. Woodward, D.B. Miracle, Acta Mater. 61 (5) (2013) 1545–1557.
[32] Y. Chen, Z. Xu, M. Wang, Y. Li, C. Wu, Y. Yang, Mater. Sci. Eng. A 792 (2020) 139774.
[33] T.-d. Huang, S.-y. Wu, H. Jiang, Y.-p. Lu, T.-m. Wang, T.-j. Li, Int. J. Miner. Metall. Mater. 27 (10) (2020) 1318–1325.
[34] O. Senkov, S. Senkova, D. Miracle, C. Woodward, Mater. Sci. Eng. A 565 (2013) 51–62.
[35] D. King, S. Cheung, S.A. Humphry-Baker, C. Parkin, A. Couet, M. Cortie, G. Lumpkin, S. Middleburgh, A.J. Knowles, Acta Mater. 166 (2019) 435–446.
[36] X. Chen, Q. Wang, Z. Cheng, M. Zhu, H. Zhou, P. Jiang, L. Zhou, Q. Xue, F. Yuan, J. Zhu, X. Wu, E. Ma, Nature 592 (7856) (2021) 712–716.
[37] R. Zhang, S. Zhao, J. Ding, Y. Chong, T. Jia, C. Ophus, M. Asta, R.O. Ritchie, A.M. Minor, Nature 581 (7808) (2020) 283–287.
[38] S. Zhao, J. Ph. Equilibria Diffus. 42 (5) (2021) 578–591.
[39] S. Zhao, Phys. Rev. Mater. 5 (10) (2021) 103604.
[40] B. Xing, X. Wang, W.J. Bowman, P. Cao, Scr. Mater. 210 (2022) 114450.
[41] Z. Su, T. Shi, H. Shen, L. Jiang, L. Wu, M. Song, Z. Li, S. Wang, C. Lu, Scr. Mater. 212 (2022) 114547.
[42] P.E. Blöchl, Phys. Rev. B 50 (24) (1994) 17953.
[43] M. Ernzerhof, G.E. Scuseria, J. Chem. Phys. 110 (11) (1999) 5029–5036.
[44] A. Zunger, S.-H. Wei, L. Ferreira, J.E. Bernard, Phys. Rev. Lett. 65 (3) (1990) 353.
[45] M.C. Gao, C. Niu, C. Jiang, D.L. Irving, in: High-Entropy Alloys, Springer, 2016, pp. 333–368.
[46] A. Van De Walle, M. Asta, G. Ceder, Calphad 26 (4) (2002) 539–553.
[47] A. Tamm, A. Aabloo, M. Klintenberg, M. Stocks, A. Caro, Acta Mater. 99 (2015) 307–312.
[48] J. Beeler Jr, R. Johnson, Phys. Rev. 156 (3) (1967) 677.
[49] B. Widom, J. Chem. Phys. 39 (11) (1963) 2808–2812.
[50] M. Cerdeira, S. Palacios, C. González, D. Fernandez-Pello, R. Iglesias, J. Nucl. Mater. 478 (2016) 185–196.
[51] D. Connétable, J. Huez, E. Andrieu, C. Mijoule, J. Phys. 23 (40) (2011) 405401.
[52] J. Hou, Y.-W. You, X.-S. Kong, J. Song, C. Liu, Acta Mater. 211 (2021) 116860.
[53] R. Johnson, Phys. Rev. B 39 (17) (1989) 12554.
[54] H. Wadley, X. Zhou, R. Johnson, M. Neurock, Prog. Mater. Sci. 46 (3–4) (2001) 329–377.
[55] D.-Y. Lin, S. Wang, D. Peng, M. Li, X. Hui, J. Phys. 25 (10) (2013) 105404.
[56] X.W. Zhou, H.N.G. Wadley, R.A. Johnson, D.J. Larson, N. Tabat, A. Cerezo, A.K. Petford-Long, G.D.W. Smith, P.H. Clifton, R.L. Martens, T.F. Kelly, Acta Mater. 49 (19) (2001) 4005–4015.
[57] J.R. Morris, C. Wang, K. Ho, C.T. Chan, Phys. Rev. B 49 (5) (1994) 3109.
[58] C. Liu, G. Li, Y. Liang, A. Wu, Phys. Rev. B 71 (6) (2005) 064204.
[59] Y. Li, Q.-H. Hao, Q.-L. Cao, C. Liu, Phys. Rev. B 78 (17) (2008) 174202.
[60] J. Cowley, Phys. Rev. 77 (5) (1950) 669.
[61] X. Zhang, M.H. Sluiter, Phys. Rev. B 91 (17) (2015) 174107.
[62] D.C. Ford, P. Zapol, L.D. Cooley, J. Phys. Chem. C 119 (26) (2015) 14728–14736.
[63] D.R. Mason, D. Nguyen-Manh, C.S. Becquart, J. Phys. 29 (50) (2017) 505501.
[64] M. Gilbert, S. Dudarev, P. Derlet, D. Pettifor, J. Phys. 20 (34) (2008) 345214.
[65] A. Semenov, C. Woo, Phys. Rev. B 66 (2) (2002) 024118.
[66] F. Gao, D. Bacon, P. Flewitt, T. Lewis, Model. Simul. Mater. Sci. Eng. 6 (5) (1998) 543.
[67] D. Bacon, F. Gao, Y.N. Osetsky, J. Nucl. Mater. 276 (1–3) (2000) 1–12.